Rapid Access to Ground- and Excited-State Properties of Gold Nanoclusters Coated with Organic Ligands: Evaluation of the DFTB Method Performance

Khaoula Maghrebi, Isaac Chantrenne, Sabri Messaoudi, Thomas Frauenheim, Arnaud Fihey, Carlos R Lien-Medrano

Rapid Access to Ground and Excited State Properties of Gold Nanoclusters Coated with Organic Ligands: Evaluation of the DFTB Method Performance

Khaoula Maghrebi,[†,‡,△] Isaac Chantrenne,[¶] Sabri Messaoudi,[†,‡,§] Thomas Frauenheim,[‖,⊥,#] Arnaud Fihey,[*,¶] and Carlos R. Lien-Medrano[*,@,△]

†*Faculty of Sciences of Bizerte FSB, Carthage University , 7021 Jarzouna, Tunisia*
‡*Laboratory of Materials, Molecules and Applications, IPEST, Carthage University, Sidi Bou Said Road, B.P. 51 La Marsa- 2070, Tunisia*
¶*Univ Rennes, CNRS, ISCR (Institut des Sciences Chimiques de Rennes) - UMR 6226, F-35000 Rennes, France*
§*Department of Chemistry, College of Science, Qassim University, Buraidah 51452, Saudi Arabia*
‖*Constructor University, School of Science, Campus Ring 1, 28759 Bremen, Germany*
⊥*Beijing Computational Research Center (CSRC), 100193 Beijing, China*
#*Shenzen JL Computational Science and Applied Research Institute (CSAR), 518110 Shenzhen, China*
@*Bremen Center for Computational Materials Science (BCCMS), Universität Bremen, 28359 Bremen, Germany*
△*Contributed equally to this work*

E-mail: arnaud.fihey@univ-rennes1.fr; cmedrano@unc.edu.ar

Abstract

Gold nanoclusters stand as promising building blocks for solar energy harvesting applications, luminescent materials and catalytic devices. At the frontier between molecular and metallic structures, their large number of electrons prevent the use of *ab intio* quantum mechanic method to rationalize and predict their structure-property relationships, especially when fully coated with organic ligands. Using an approximate DFT-based scheme, namely Tight-Binding Density Functional (DFTB), we demonstrate that is possible to rapidly access the ground (geometry and electronic structure) and excited state (UV-Visible absorption) properties of these nano-objects without sacrificing the qualitative accuracy of its parent DFT, paving the way towards a quantum material design of gold-organic nano-devices.

Keywords

Nanocluster, quantum chemistry, tight-binding, optical properties

Introduction

Thiolate-protected gold nanoclusters (GNC), consisting of a gold metal core stabilized by a thiolate-ligands layer $Au_x(SR)_y$ (where x and y represent gold atoms and surface ligands numbers, respectively), have attracted considerable attention in recent years. Their molecular, strong size-dependent behavior, stability, and tunability of properties,[1–3] make them potentials building blocs for solar energy harvesting devices,[4,5] especially when the coat of organic ligands around the cluster not only protects the metal but also possesses photochemical properties. They are also considered as efficient catalyst,[1,6,7] and serve as fluorescent probes for biomedical applications.[8,9]

Single crystal X-ray diffraction has been used to characterize a vast number of GNCs, owing to their highly symmetrical structures. Some of the typical and most investigated GNCs are listed below. Among the most frequently studied systems is the $Au_{25}(SR)_{18}$ cluster, which has been extensively researched.[10] To synthesize the $Au_{25}(SR)_{18}$ cluster, a range of thiolate ligands has been employed, including SC_nH_{2n+1}, glutathione, SC_2H_4Ph, and thiols with a polymerizable group.[10,11] The native $Au_{25}(SR)_{18}$ cluster is negatively charged, with the n-tetraoctylammonium cation (TOA^+) serving as the counterion.[2,12,13] The $[Au_{25}(SR)_{18}]^-$ cluster can be readily oxidized to $[Au_{25}(SR)_{18}]^0$ and to $[Au_{25}(SR)_{18}]^+$ by chemical oxidation.[2,10,12,14–16] $Au_{38}(SR)_{24}$ nanoclusters have garnered significant attention, with several theoretical models proposed to describe their structural arrangement. These models suggest that the gold core of these clusters may either be symmetric or disordered.[17,18] Interestingly, the unit cell of $Au_{38}(SC_2H_4Ph)_{24}$ does not contain a counterion, indicating that the cluster is neutral in nature.[19] In addition, several studies have investigated the impact of different thiol ligands on the electrochemical and thermodynamic stability of these nanoclusters.[20–22] Of the various thiol ligands, $–SC_2H_4Ph$ thiol is particularly appealing due to its high electrochemical and thermodynamic stability, as demonstrated by Jung *et al.*[20] Recently, Jadzinsky et al. reported a complete structural characterization of thiolate-protected Au_{102}(p-MBA)$_{44}$ (pMBA = p-mercaptobenzoic acid, SPhCOOH).[23] The exceptional stability of the Au_{102}(p-MBA)$_{44}$ nanocluster may be attributed in part to the electronic shell closing effect, which results from the effective presence of 58 valence electrons (102-44).[23,24] Finally, $Au_{144}(SR)_{60}$ has gained significant attention as one of the largest molecular-like GNC. The Au–S framework of $Au_{144}(SR)_{60}$ was initially predicted by density functional theory (DFT) calculations in 2009,[25] and the experimental structure was not published until almost a decade later, in 2018.[26]

To understand the deep structure-properties relationship in GNCs, DFT has been employed in theoretical studies for over a decade.[27,28] While numerous theoretical works have been conducted on small and medium-sized thiolate-protected gold clusters, they often overlook a portion or the entirety of the ligand coat.[2] Very few DFT-based studies have been performed on large-size thiolate-protected gold clusters,[24,29] where investigating the excited state properties with TD-DFT is still nowadays a very computationally demanding task. As an alternative, the use of cheaper quantum mechanics models is relevant to achieve a complete description of these nano-objects without neglecting the organic coat, reaching up to thousands of atoms. Among such approximate models, the Density Func-

[0a] *Faculty of Sciences of Bizerte FSB, Carthage University , 7021 Jarzouna, Tunisia*

[0b] *Laboratory of Materials, Molecules and Applications, IPEST, Carthage University, Sidi Bou Said Road, B.P. 51 La Marsa- 2070, Tunisia*

[0c] *Bremen Center for Computational Materials Science (BCCMS), Universität Bremen, Germany*

[0d] *Univ Rennes, CNRS, ISCR (Institut des Sciences Chimiques de Rennes) - UMR 6226, F-35000 Rennes, France*

[0e] *Department of Chemistry, College of Science, Qassim University, Buraidah 51452, Saudi Arabia*

[0f] *Beijing Computational Research Center (CSRC), Beijing, China*

[0g] *Shenzen JL Computational Science and Applied Research Institute (CSAR), Shenzhen, China*

tional Tight-Binding (DFTB) framework has become a popular choice.

DFTB is a DFT-based approximate method in which a combination of a minimal basis set and the neglect/parameterization of the two-electron integrals (by pre-computing them at the DFT/PBE level of theory and tabulating them as numbers) allow to solve the Kohn-Sham equations while saving 99% of the calculation cost. The modern version of DFTB is the so-called self-consistent charges DFTB (SCC-DFTB)[30] in which the variation of the atomic charges is taken into account iteratively while searching for the answer of the tight-binding problem, allowing charge-transfer to occur within atoms/molecules/material. The self-consistent variation of the DFTB electronic energy with respect to charges is determined with the help of a second (SCC-DFTB2)[30] or a third order (SCC-DFTB3)[31] Taylor expansion starting form a reference density corresponding to the sum of neutral atomic densities. The performance of DFTB methods is thus principally driven by the quality of the created parameters for a specific application. In a previous work, we designed a set of SCC-DFTB2 parameters for the description of gold-thiolates interaction, encompassing Au, S, C, N, H, O atoms.[32] The *auorg* set of parameters, while encompassing the required pair potentials for the description of thiolate protected GNCs, have been primarily tested on the electronic structure and geometry of gold bulk, surfaces or slabs decorated with organic molecules,[32] and bare gold nanoparticles of growing sizes.[33,34] Optical properties of such gold nanoparticles were computed in another work, taking advantage of TD-DFT electron dynamics simulation to compute the plasmon resonance band and rationalize their characteristics.[34]

The *auorg* parameter set was not originally developed for an specific application on GNCs, which exhibit a complex core-shell atomic structure that includes gold atoms with different coordination numbers and various S-Au bonding arrangements that depend on cluster size and shape. As a result, the accuracy of a parameter-based computational framework must be carefully evaluated in different scenarios. Nevertheless, the *auorg* parameters have already been used to describe a fluorophore-functionalized GNC and rationalize the photoinduced electron transfer in the nano-objects.[35] Recently, phosphorus parameters were added to enable modeling of phosphate-protected GNCs.[36]

In this work, we provide a comprehensive evaluation of the capability of DFTB using the *auorg* parameters, to accurately describe the structural and electronic properties of various thiolate-protected GNCs, namely $Au_{25}(SR)_{18}^-$, $Au_{38}(SR)_{24}$, $Au_{102}(SR)_{44}$ and $Au_{144}(SR)_{60}$ (see Figure 1(a) and (b)). A specific focus is set on analysing how the nature of the protecting thiol ligands influence the GNC properties. For the first time we also explore the ability of TD-DFTB, both linear-response formalism in the frequency domain[37] and through real-time formalism,[38] to retrieve the experimental UV-Visible absorption spectra and provide a rationalisation of the absorption bands nature. These results are also confronted to previously computed TD-DFT spectra. Through this study we point out the identified strengths and weaknesses of the current *auorg* set in order to facilitate future applications and/or re-parameterization of SCC-DFTB2 for these nano-objects.

Computational methods

Geometries of the GNCs were fully optimized without symmetry restrictions using their experimental crystal structure as the starting geometry. Following geometry optimization, frequency calculations were performed, resulting in only positive eigenvalues. The ground state electronic structures and geometries of all the systems studied were obtained using the self-consistent-charge density-functional-tight-binding (SCC-DFTB).[30,39,40] Particularly, we used the DFTB+ code,[41] with the *auorg* set of parameters[32] in the second-order SCC-DFTB for all the DFTB calculations presented in this work.

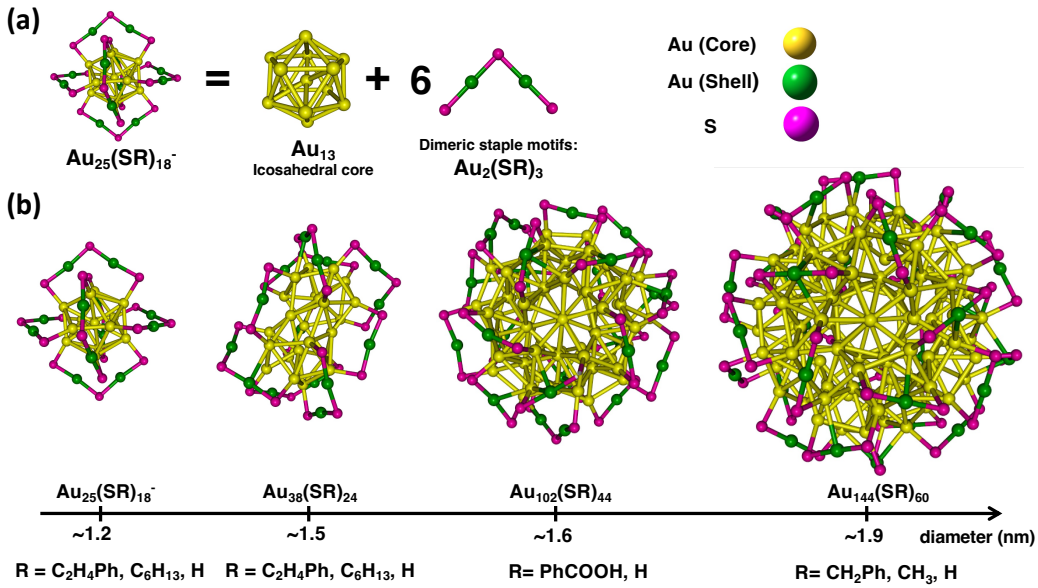

Figure 1: (a) Core-shell representation of a thiolated gold nanocluster. $Au_{25}(SR)_{18}^-$ was taken as an example for the representation. (b) Representation of the systems under study: $Au_{25}(SR)_{18}^-$, $Au_{38}(SR)_{24}$, $Au_{102}(SR)_{44}$ and $Au_{144}(SR)_{60}$ nanoclusters with different protecting ligands R. All R moieties are omitted for clarity.

Using these equilibrium geometries, the optical properties were simulated through the time-dependent DFTB (TD-DFTB) framework within two different approaches: the Casida's formalism[42] or linear-response (denoted here LR-TD-DFTB) and the real-time propagation of the single electron density matrix (RT-TD-DFTB).[38] In LR-TD-DFTB, the electronic excitation energy ω_I is obtained from solving the following eigenvalue problem:

$$\Omega \mathbf{F}_I = \omega_I^2 \mathbf{F}_I. \quad (1)$$

Here, Ω is the response matrix and its elements in the implementation from Niehaus et al. within the DFTB method[37] are

$$\Omega_{ij\sigma,kl\tau} = \delta_{ik}\delta_{jl}\delta_{\sigma\tau}\omega_{ij}^2 + 2\sqrt{\omega_{ij}}K_{ij\sigma,kl\tau}\sqrt{\omega_{kl}}, \quad (2)$$

where σ and τ are spin indices, $\omega_{ij} = \varepsilon_j - \varepsilon_i$, i,k and j,l are occupied and unoccupied KS orbitals respectively, whereas K is the so-called coupling matrix. The huge advantage of the LR-TD-DFTB formalism implementation[37] is the monopole approximation, i.e. the truncation at the first order of the multipole expansion of the transition density, in which coupling matrix elements $K_{ij\sigma,kl\tau}$ assume simple expressions, thus reducing the computational cost. Once the eigenvalue problem from equation 1 is solved within TD-DFTB, the oscillator strength f^I for the transition I can be calculated as

$$f^I = \frac{2}{3}\sum_{p=1}^{3}\left|\sum_{ij\sigma}\langle\psi_{i\sigma}|\hat{r}_p|\psi_{j\sigma}\rangle\sqrt{\omega_{ij\sigma}}F^I_{ij\sigma}\right|^2, \quad (3)$$

where $\hat{r}_p$ stands for the p-th component of the position operator. In this way, the absorption spectrum can be obtained from the convolution of the discrete excitation energies ω_I with a Lorentzian function weighted by the corresponding oscillator strength f^I.

In the RT-TD-DFTB approach,[38] we obtain the excitation energies ω and intensities using a different protocol, however, obtaining equivalent results (*vide infra*). First, a *kick* perturbation is applied to the ground state single-electron density matrix ρ_0, i.e. a Dirac-delta electric field pulse $\mathbf{E}_{kick}(t) = \mathscr{E}_0\delta(t)\hat{\mathbf{e}}$ polarized in direction $\hat{\mathbf{e}} \in \{\hat{i},\hat{j},\hat{k}\}$, which excites all dipole-allowed transitions.[43] After the perturbation, the evolution of ρ can be calculated by numerical integration of the Liouville-von

Neumann equation of motion, which in a non-orthogonal basis is

$$\dot{\rho} = -\mathrm{i}(S^{-1}H\rho - \rho H S^{-1}), \tag{4}$$

where ρ is the single-electron density matrix, H is the SCC-DFTB Hamiltonian and S^{-1} is the inverse of the overlap matrix. During the time evolution of the system its time-dependent dipole moment contains information about the excited frequencies and oscillator strengths. To access this information we need to Fourier transform the dipole moment signal along each cartesian direction after the excitation and then find the frequency-dependent polarizability tensor following[44]

$$\boldsymbol{\alpha}(\omega) = \frac{\boldsymbol{\mu}(\omega) - \boldsymbol{\mu}_0}{\mathscr{E}_0}, \tag{5}$$

where $\boldsymbol{\mu}_0$ is the net dipole moment of the system and $\mathscr{E}_0$ is the Dirac-delta (scalar) field strength. Once obtained the polarizability $\boldsymbol{\alpha}(\omega)$, the absorption cross-section $\sigma(\omega)$ is proportional to the imaginary part of the latter[45]

$$\sigma(\omega) = \frac{4\pi\omega}{c}\mathrm{Im}(\bar{\alpha}(\omega)), \tag{6}$$

where $\bar{\alpha}(\omega) = \frac{1}{3}\mathrm{Tr}[\boldsymbol{\alpha}(\omega))]$. By changing the perturbation added to the Hamiltonian to a continuos laser type $\mathbf{E}_{laser}(t) = \mathscr{E}_0 \sin(\omega t)\mathbf{r}$, one can study the excitation processes under illumination. In this case ω is the transition of interest and the laser is applied in tune with the transition dipole vector direction $\mathbf{r}$. The latter can be calculated as the second rank polarizability tensor at the energy of interest ω. After diagonalization of the tensor, the corresponding eigenvector with the largest eigenvalue represents the maximal polarizability direction and can be associated with the transition dipole moment vector.

In addition, single point DFT calculations have been conducted on the DFTB relaxed geometries, in order to assess the quality of the electronic structure (density of states, electronic gaps). These DFT values have been obtained with the PBE functional, associated to a 6-31G(d,p) basis set for C, N, O, S and H atoms and a LANL2DZ basis set and pseudopotential for Au atoms, and have been conducted with the Gaussian 16 software.[46] All computations have been conducted in vacuum. This DFT level of theory has been chosen in order to be the closest to the quantum model used in SCC-DFTB2, i.e., a GGA functional with a small basis set.

Results and discussion

Systems under study.

In the following we detail the structure and properties of four GNCs of growing size, namely $Au_{25}(SR)_{18}^-$, $Au_{38}(SR)_{24}$, $Au_{102}(SR)_{44}$ and $Au_{144}(SR)_{60}$ (Figure 1 (b)). The -R protecting ligands are chosen to match the experimental conditions: phenylethyl ligands for $Au_{25}(SR)_{18}^{-2}$ and $Au_{38}(SR)_{24}$,[19] pMBA (= para-mercaptobenzoic acid) for $Au_{102}(SR)_{44}$[47] and methylphenyl for $Au_{144}(SR)_{60}$.[26] For these clusters, their molecular-like electronic structure define their optical response and localized surface plasmon resonance is not expected to dominate the experimental absorption features.[26] In the following we briefly recall the structure of the GNC under study, and the reader should refer to the cited works for more detailed descriptions.

- $Au_{25}(SR)_{18}^-$ exhibits a core-shell structure, that is, an icosahedral Au_{13} core capped by a Au_{12} shell consisting of six "staple-like" motifs of -S(R)-Au-S(R)-Au-S(R)- ($Au_2(SR)_3$), where three sulfur and two gold atoms are arranged in a "V-shaped" pattern (Figure 1 (a)).[2,10,12] The $Au_{25}(SR)_{18}$ framework adopts a quasi-D_{2h} symmetry.[2,13]

- The $Au_{38}(SR)_{24}$ GNC exhibit a face-fused biicosahedral Au_{23} core, which is covered by three monomeric staples –SR–Au–SR– ($Au(SR)_2$) at the waist of the Au_{23} rod and six dimeric staples –SR–Au–SR–Au–SR– ($Au_2(SR)_3$) with three on the top icosahedron and other three on the bottom icosahedron. The six $Au_2(SR)_3$ staples are arranged

in a staggered configuration, and the $Au_{38}(S)_{24}$ framework has a C(3) rotation axis. The Au_{23} core adopts a quasi-D_{3h} symmetry (see Figure 1 (b)).[19]

- The atomic structure of Au_{102}(p-MBA)$_{44}$ consists of an approximately D_{5h}-symmetric Au_{79} metallic core with a protective gold-thiolate layer Au_{23}(p-MBA)$_{44}$.[48] This nanocluster possesses a core of Au_{79} and a shell of $Au_{23}(SR)_{44}$. The $Au_{23}(SR)_{44}$ shell is composed of 19 monomers (-SR-Au-SR-) and 2 dimers (-SR-Au-SR-Au-SR-), imposing C_2 symmetry on the entire nanocluster.[23,47](See Figure 1 (b)).

- The $Au_{144}(SR)_{60}$ cluster consists of an icosahedral Au_{114} core with 30 equivalent RS-Au-SR oligomers protecting its surface[25] (see Figure 1 (b)). Several groups reported crystals of Au_{144} nanoparticles with various ligands, including SC_2H_4Ph and p-MBA.[49,50] The experimental structure of $Au_{144}(SR)_{60}$ has high symmetry with 6 C_5 rotation axes, 10 C_3 rotation axes, and 15 C_2 rotation axes.[26]

Ground state geometries of $Au_x(SR)_y$

Table 1 presents a comparison of the average distances and angles obtained using DFTB with X-ray crystallographic data. Additionally, the coordinates of the DFTB optimized structures are provided online as supplementary *.xyz* files. Table S1 present in addition a comparison between our DFTB results and DFT structures from previous works in the literature.

In all cases the experimental structure of the cluster described above is retrieved, though variations in the accuracy of the Au-Au and Au-S bond distances are observed depending on the type of bonds (Table 1). Au-Au (core) mean bond distances are slightly underestimated by ca. 0.1 Å for the smallest clusters, $Au_{25}(SC_2H_4Ph)_{18}^-$ and $Au_{38}(SC_2H_4Ph)_{24}$ where the gold core is very molecular-like and far from a bulk environment. On the opposite, for larger clusters Au_{102}(p-MBA)$_{44}$ and $Au_{144}(SCH_2Ph)_{60}$, the mean computed Au-Au distance is almost identical to the experimental one, and reaches the bulk Au-Au distance of 2.88 Å. These conclusions overlap with the observation made in the original parameterization work on the description of bare Au_n clusters.[32] The largest deviation is observed in all clusters for bond distances between atoms from the core and from the shell (Au-

Table 1: Comparison of the experimental and DFTB average distances (in Angströms) and angles (in degrees) within the GNCs. RMSD values represent the mean deviation of the Au and S atoms positions (in Angströms) compared to the crystallographic structure.

$Au_{25}(SC_2H_4Ph)_{18}^-$	DFTB	Exp.[2]
Au(core)-Au(core)	2.77	2.88
Au(shell)-S(shell)	2.39	2.31
Au(core)-Au(shell)	3.50	3.16
Au(core)-S(shell)	2.61	2.37
S-Au-S	177.1	172.3
Au-S-Au	101.5	100.9
RMSD	0.39	
$Au_{38}(SC_2H_4Ph)_{24}$	DFTB	Exp.[19]
Au(core)-Au(core)	2.81	2.89
Au(shell)-S(shell)	2.39	2.30
Au(core)-Au(shell)	3.47	3.19
Au(core)-S(shell)	2.59	2.37
S-Au-S	175.0	171.5
Au-S-Au	100.4	101.1
RMSD	0.35	
Au_{102}(p-MBA)$_{44}$	DFTB	Exp.[47]
Au(core)-Au(core)	2.85	2.87
Au(shell)-S(shell)	2.44	2.41
Au(core)-Au(shell)	3.09	3.08
Au(core)-S(shell)	2.61	2.38
S-Au-S	160.2	164.4
Au-S-Au	112.5	122.6
RMSD	0.39	
$Au_{144}(SCH_2Ph)_{60}$	DFTB	Exp.[26]
Au(core)-Au(core)	2.88	2.89
Au(shell)-S(shell)	2.43	2.30
Au(core)-Au(shell)	3.05	3.18
Au(core)-S(shell)	2.62	2.41
S-Au-S	165.4	not given
RMSD	0.51	

S and Au-Au). Values computed at the DFTB level are typically overestimated by ca. 0.3 Å. Computed S-Au-S and Au-S-Au angles are in satisfying agreement with the experimental ones, showing deviation ranging between 1 and 10 degrees at most. The Au-S-Au angle for $Au_{102}(p\text{-}MBA)_{44}$ is the farthest from the X-Ray structure, at 112.5° instead of 122.6°. In a more general way, when increasing the size of the cluster, the deviation between the DFTB structure and the X-Ray data remains similar. The RMSD (root mean square deviation) value (on the Au and S positions) only slightly increase from 0.39 Å for $Au_{25}(SC_2H_4Ph)_{18}^-$ to 0.51 Å for $Au_{144}(SCH_2Ph)_{60}$. Globally, for all studied GNCs, the structures optimized at the DFTB level exhibit low RMSD values compared to the crystal structures, and for instance performs as well as a recent dedicated algorithm designed for GNC structure search.[51] Nevertheless, one can see that the DFTB structure of the smaller GNC present the most important deviations to experiments. This arises from the intrinsic discrepancy in their molecular bond environment, while on the opposite, larger GNCs present more homogeneous bond distances, that are easier to reproduce with our approximate method.

When comparing the DFTB structures to DFT results (see Table S1), obtained with the PBE functional for $Au_{25}(SH)_{18}^-$,[2] $Au_{38}(SCH_3)_{24}$,[18] $Au_{102}(Sp\text{-}MBA)_{44}$[52] and with a LDA functional for $Au_{144}(SCH_3)_{60}$,[25] tendencies can be identified. Firstly, when DFTB shortens the Au-Au distance of the core for the two smaller clusters (as described above) DFT studies on the opposite reported an overestimation of these bondlengths, by 0.05 Å to 0.1 Å. Interestingly for the two larger clusters, this DFT overestimation is still present, while DFTB converges to the expected XR distances, around 2.88 Å. Secondly, the overestimation of the core-shell (Au-Au/Au-S) bondlengths observed with DFTB is also present in the reported DFT structures of all the clusters, although to a lesser extent. For instance, Au-Au and Au-S distances are overestimated by PBE by 0.13 Å and 0.11 Å, respectively, in $Au_{25}(SH)_{18}^-$ compared to the experimental data.[2] Angles are globally obtained with very small deviations to DFT through the series. Of course, the DFT results can be quite straightforwardly improved by selecting the appropriate functional/basis set, while increasing the DFTB accuracy would require a new parameterization work, for instance by dividing the gold parameters into two *types* of gold atoms corresponding to the core and the shell region, that do not possess the same chemical environment, and render difficult the description of the GNC with a unique DFTB set.

As a final remark, it is observed that the geometries are only slightly impacted by the nature of the protecting ligands, as shown in Table S1 for other types of coating inspired by experimental or theoretical works, namely methyl,[20,24,25,53] hexyl,[20,54,55] or by simplifying each ligand with a sole H atom.[2,27,28] The electronic structure analysis and properties calculations presented in this work are based on the DFTB ground-state optimized geometries discussed above.

Electronic structure of $Au_x(SR)_y$

In this section we analyze the DFTB electronic structures obtained on the corresponding relaxed geometries of the different GNCs. These structures are also used to performed DFT single point calculations at the GGA level (see Computational details), thus serving as a reference to assess the impact of the TB approximations on the electronic structures. The HOMO-LUMO energy gaps calculated for the GNCs provide a useful descriptor for the transition from molecular to nanoparticle-like electronic structure. When comparing to the known literature, the DFTB values for the gaps are in excellent agreement with those obtained from previous DFT works and experimental measurements. For instance, our calculated values of 1.16 eV, 0.79 eV and 0.43 eV for $Au_{25}(SC_2H_4Ph)_{18}^-$, $Au_{38}(SC_2H_4Ph)_{24}$ and $Au_{102}(p\text{-}MBA)_{44}$, respectively, are comparable the experimental and computed reported values in the literature: 1.2-1.8 eV,[2,10,56,57] 0.89-0.9 eV[10,18,58] and 0.5-0.6 eV,[20,24,48,59] respectively. In the case of $Au_{144}(SCH_2Ph)_{60}$

cluster, previous electrochemical studies have shown that it possesses almost a zero HOMO-LUMO gap, making it the smallest "metallic" Au-nanocluster without a LSPR.[60–62] In addition, Koivisto *et al.* reported an optical gap of 0.19 eV for $Au_{144}(SC_2H_4Ph)_{60}$.[63] The DFTB electronic gap value of 0.06 eV for this cluster is in good agreement with these experiments. Table S2 present a comparison of the computed DFTB electronic gaps for the different clusters with various ligands, as well as values obtained with DFT (PBE functional, see computational details for more information) for the H terminated systems at the DFTB geometry, for a more direct comparison. The DFTB values are close to the DFT ones throughout the series, yet always inferior, by 0.23 eV for $Au_{25}(SH)_{18}^{-}$, 0.21 eV for $Au_{38}(SH)_{24}$, 0.10 eV for $Au_{102}(SH)_{44}$ and 0.04 eV for $Au_{144}(SH)_{60}$. This constitutes a satisfying result, as this value is highly sensitive to any difference in the QM model.

On the overall, DFTB clearly recover the expected decrease in the electronic gap with the growing GNC size, from 1.16 eV for $Au_{25}(SC_2H_4Ph)_{18}^{-}$ to 0.06 eV for $Au_{144}(SCH_2Ph)_{60}$. The presence of ligands reduces the electronic HOMO-LUMO gaps for all the GNCs studied, compared to a model with only -H termination (see Table S2). It is worth noting that the values of energy gaps for aromatic ligands (CH_2CH_2Ph) are somewhat larger than those for aliphatic ligands (C_6H_{13}) by 0.03 eV and 0.01 eV for $Au_{25}(SR)_{18}^{-}$, $Au_{38}(SR)_{24}$ clusters respectively. As a general observation, these calculations imply that the ground-state electronic features of the GNC are only slightly influenced by the nature of the ligands.

To further detail the electronic structure of the GNCs, the density of states (DOS) and projected density of states (PDOS) are detailed in Figure 2 for the different clusters. The PDOS are plotted with the contributions of S and core and shell atoms for Au. General observations on the contribution to the DOS can be made within the series of GNCs. Firstly, it is evident that the gold atoms forming the core of the clusters always constitute the primary

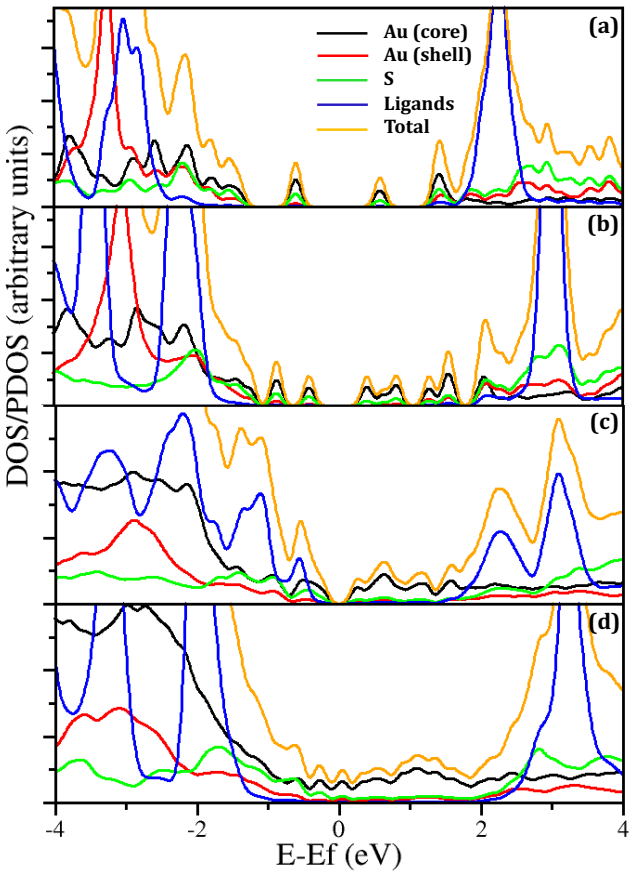

Figure 2: DFTB Density of states (DOS) and partial density of states (PDOS) of (a) $Au_{25}(SC_2H_4Ph)_{18}^{-}$, (b) $Au_{38}(SC_2H_4Ph)_{24}$, (c) Au_{102}(p-MBA)$_{44}$ and (d) $Au_{144}(SCH_2Ph)_{60}$ GNCs (with a gaussian broadening σ value of 0.1 eV). The zero of energy is set on the Fermi level.

contributions in the electronic states around the Fermi level, with a lesser involvement of the sulfur atoms. Gold atoms from the outer shell of the clusters exhibit strong involvement around 1 eV lower (resp. higher) in energy for the occupied (resp. unoccupied) states.

DOS and PDOS of the simplified H-terminated GNCs obtained with DFTB and DFT (at the DFTB geometry, see computational details) are compared in Figure S1 and S2. Firstly, The above observations concerning the core/shell contributions around the electronic gap are nicely consistent with our DFT calculations (Figure S1). Secondly, when looking at the orbital resolved PDOS of the GNCs (Figure S2), one can see that: i) the predominance of Au *d* orbitals from 1 eV be-

low the Fermi level and deeper is correctly reproduced, ii) in this region the *sp* orbitals of Au and S show a smaller involvement, and a roughly similar contribution to the states, in agreement with DFT, iii) after the Fermi level, the *sp* orbitals of gold become more involved than the *d* orbitals in both level of theory. However, clear discrepancies with DFT can be observed for sulfur contributions in high energy non-occupied states, around 2 eV above the Fermi level where the contribution of the *d* orbitals is overestimated compared to DFT, as previously reported.[35]

From Figure 2 the role of the ligands in the DFTB DOS can be visualized. For $Au_{25}(SC_2H_4Ph)_{18}^-$, $Au_{38}(SC_2H_4Ph)_{24}$ and $Au_{144}(SCH_2Ph)_{60}$ the contribution of the organic coat of phenylethyl/phenylmethyl units appears more than 2 eV before/after the fermi level. The positions of the ligands contribution in $Au_{25}(SC_2H_4Ph)_{18}^-$ are shifted to lower energy compared to their positions in the two latter GNCs, as a result of the negative charge bore by the system. For Au_{102}(p-MBA)$_{44}$, a different situation is observed, with the occupied orbitals of the p-MBA ligands found higher in energy and actually constituting the main contribution in the states of the GNC from 0.5 to 1.5 eV before the fermi level. Computed DOS with different types of ligands (see Figure S3) show that the organic units impact the electronic structure of the clusters (bands from Au/S atoms) mainly by producing a shift with respect to the H-terminated clusters.

Optical properties of $Au_x(SR)_y$

RT-TD-DFTB as a method of choice for nanoscaled systems

As discussed in the Computational Details section, two different DFTB frameworks are available to access the vertical absorption profiles. The real-time method requires running three dynamics (one per each Cartesian axis), necessitating the convergence of the dynamics parameters, such as simulation time and time step. Additionally the Fourier transform of the obtained dipole moment adds another step in the protocol to obtained the absorption spectrum. As a result, the linear-response method offers a more practical and efficient approach for analyzing systems from small to medium sizes. However, within the linear-response Casida method, as a matter of fact, the number of excitations to compute in order to cover the UV-Visible range is the limiting parameter for larger systems. Specifically, in the case of large systems with a high density of states, such as in this study, the individual excited states typically carry only a small fraction of the total oscillator strength. As a consequence, solving the eigenvalue problem becomes inefficient for those cases[64] and may lead to convergence issues. For instance, even for the smallest GNC in the series, $Au_{25}(SC_2H_4Ph)_{18}^-$, one would need to compute the 3000 first excitations to obtain the spectrum up to 4 eV (ca. 300 nm). On the other hand, RT-TD-DFTB stands as a promising alternative to the linear-response Casida method, especially for modeling larger systems. Using the kick-perturbation method, the real-time approach allows for instantaneous access to all excitations at once, which is particularly advantageous for studying hybrid systems with disparate absorption properties, such as ligand-protected GNCs. These systems exhibit transitions of the metal core in the visible range and the molecules in the UV range, which are separated by a wide energy gap. Applying the linear-response Casida method in such systems could be cumbersome since one may not confine the number of excitations to just one energy region. These two formalisms lead to the same absorption spectrum when they can both be applied. As one can see in Figure S4 in the case of $Au_{25}(SC_2H_4Ph)_{18}^-$ and $Au_{38}(SC_2H_4Ph)_{24}$, the LR-TD-DFTB and the RT-TD-DFTB formalism result exactly in the same spectra, while the computations are a lot more efficient in the case of the RT model. As a rule of thumb, for this series of GNCs, we found that the computation time necessary to model the UV-Visible absorption spectra with LR-TD-DFTB is at least one order of magnitude larger than when using the RT-TD-DFTB framework. Based on these considerations, the absorption profiles are in all

cases computed at the RT-TD-DFTB level in the following.

Optical spectra analysis

On Figure 3 can be seen the computed absorption spectra of the four GNCs studied. The clusters size, *i.e.* the total number of atoms, has a direct impact on the density of states in the electronic structure, as shown in Figure 2), resulting in a difference in the number of possible electronic transitions. This alters the shape of the UV-Visible absorption profile within the series, from a molecular-like spectrum shape for the $Au_{25}(SC_2H_4Ph)_{18}^-$ and $Au_{38}(SC_2H_4Ph)_{24}$ (Figure 3 (a) and (b), respectively), to a semiconductor-like spectrum shape in the case of Au_{102}(p-MBA)$_{44}$ and $Au_{144}(SCH_2Ph)_{60}$ (Figure 3 (c) and (d), respectively). The first two GNCs in the series show clear sharp transitions in the spectrum, while the two bigger clusters exhibit wide bands with increasing absorption from approximately 0.5 eV.

The experimental absorption spectrum of $Au_{25}(SC_2H_4Ph)_{18}^-$ in toluene shows at least three well-defined bands at 1.8 eV, 2.75 eV, and 3.1 eV.[2] The calculated spectrum of $Au_{25}(SC_2H_4Ph)_{18}^-$ in Figure 3 (a) agrees qualitatively, especially in the spectral shape and number of bands with the mentioned measurements (see Figure S5 (a) and (c) for a direct comparison with the experiment). An homogeneous red shift can be observed leading to transitions at lower energies in comparison with the experiments, which can be attributed to an intrinsic limitation of the parameterization, based on DFT integrals computed at the PBE level.[32] Previous DFT works have indeed shown that most GGA functionals lead to predictions for the first peaks that are shifted to the red compared to experiments.[27,28] Actually, most of the theoretical works in the literature use a simpler model, namely $Au_{25}(SH)_{18}^-$ to speed-up the TD-DFT calculations. Manzhou Zhu, *et al.* have performed calculations using the SAOP potential and TZP basis set on this model system. They predicted 3 main bands at 1.52, 2.63 and 2.91 eV,[2] showing an acceptable agreement with our (red shifted) DFTB results at 1.29, 2.05 and 2.25 eV. As expected, the numbers are closer when we compare with the RT-TD-DFTB results for the $Au_{25}(SH)_{18}^-$ model at 2.39 and 2.61 eV (see Figure S5 (a) and (b) for a direct comparison with the mentioned $Au_{25}(SH)_{18}^-$ model).

Tsunoyama et al. showed for the first time that $Au_{38}(SC_{12}H_{25})_{24}$ exhibits experimentally a $\sim$ 0.9 eV optical absorption edge and a major absorption peak near 2.0 eV.[65] The UV-vis absorption spectrum of $Au_{38}(SC_2H_4Ph)_{24}$ obtained by Qian *et al.* shows a series of peaks at 1.18 eV, 1.66 eV, 2.00 eV, 2.21 eV, 2.39 eV and 2.53 eV.[58] The simulated absorption spectrum of $Au_{38}(SC_2H_4Ph)_{24}$ shown in Figure 3(b) is in good agreement with these experimental results taking into account a red-shift of the whole spectrum of ca. 0.2 eV. For instance, the lower energy band absorption appears at 0.96 eV (see inset in Figure 3 (b)). This can be seen in a direct comparison with the experiment in Figure S7. The figure also shows a comparison with the theoretical spectrum obtained by Pei, et al., using a TD-DFT approach at PBE/TZVP level of theory for a $Au_{38}(SCH_3)_{24}$ model.[18] They predicted 4 main peaks at 1.0, 1.34, 1.69 and 1.98 ev, which are in quantitatively good agreement with our results at 0.96, 1.30, 1.61, 1.80 eV.

The UV-Vis spectrum of Au_{102}(p-MBA)$_{44}$ nanocluster calculated with RT-TD-DFTB (see Fig. 3 (c)) appears, in principle, as a featureless curve within the plotted energy range with a wide an increasing absorption starting at $\sim$0.5 eV, consistent with the experimental reported spectra by Levi-Kalisman, et al.[66] and Chen et al.[59] It is worth to mention that the peak attributed experimentally to the p-MBA ligand[66] can also be seen when plotting the absorbance further in the UV region (*vide infra*). In a closer view of the spectrum it can be seen that the first absorption peak appears at 0.46 eV (see inset in Fig. 3(c)) similarly to the reported experimental absorption band edge of 0.6 eV for $Au_{102}(SPh)_{44}$,[59] and quite close to the calculated value of 0.5 eV by Hulkko *et al.* using a linear-response TD-DFT method with

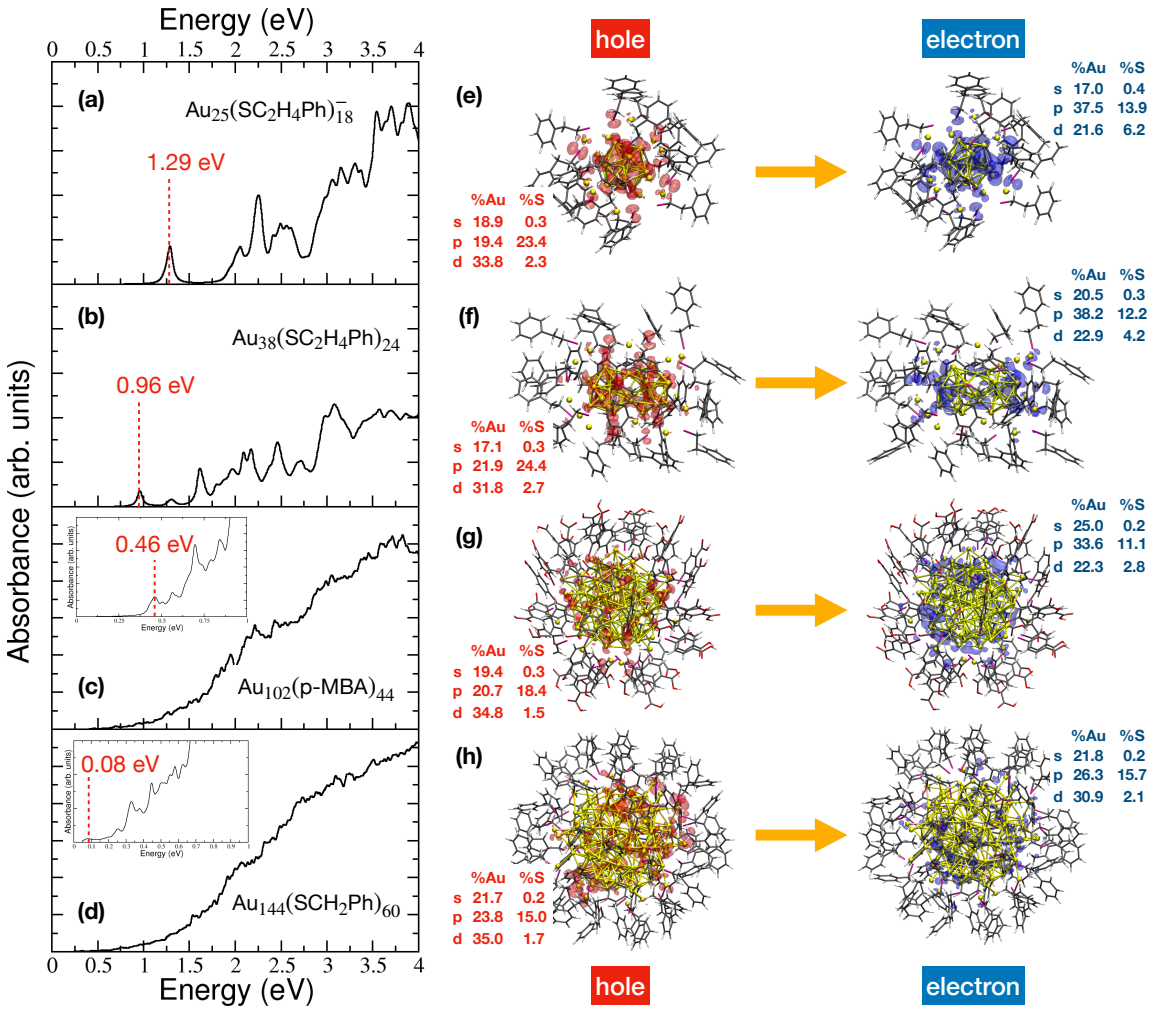

Figure 3: Absorption spectra and hole/electron densities. Simulated absorption spectra and hole/electron densities for all the systems studied: $Au_{25}(SC_2H_4Ph)_{18}^-$ (a) and (e) (isovalue = 5.10^{-4}), $Au_{38}(SC_2H_4Ph)_{24}$ (b) and (f) (isovalue = 5.10^{-4}), Au_{102}(p-MBA)$_{44}$ (c) and (g) (isovalue = 3.10^{-4}) and $Au_{144}(SCH_2Ph)_{60}$ (d) and (h) (isovalue = 2.10^{-4}), respectively. For the simulation of the absorption spectra a time step of 0.0048 fs and a field strength of 0.001 a.u. (equivalent to 1.33x10^7 W/cm^2) were used. The simulations were carried out up to 20000 steps in the case of $Au_{25}(SC_2H_4Ph)_{18}^-$ and $Au_{38}(SC_2H_4Ph)_{24}$, and up to 40000 steps for Au_{102}(p-MBA)$_{44}$ and $Au_{144}(SCH_2Ph)_{60}$. The hole/electron densities correspond to a snapshot at 90 fs of the electron dynamics.

the PBE functional.[67] A deeper view at higher energies between 1.5 eV and 3 eV (see Figure S7) shows that our results are also in good agreement with the four bands predicted by Hulkko, *et al.*.

In the case of the largest GNC $Au_{144}(SCH_2Ph)_{60}$, we found a wide broad absorption (see Figure 3 (d)) that goes far in the IR region as can be expected for an almost no-gap cluster (*vide supra*), in accordance with the experimental measurements that show a featureless decay-like absorption.[68,69] Furthermore, following the discussion proposed by Weissker *et* al., it is possible to see a fine structure of the spectrum in the visible region that is consistent with the low-temperature absorption spectra and real-time TD-DFT calculations at the PBE level of theory.[53] In Figure S8 (a), we show a direct comparison of the spectrum with the one obtained by Sinha-Roy, *et al.*[29] using real-time TD-DFT at the PBE level of theory. In principle, our spectrum shows a similar structure

between 1 and 4.5 eV with a higher density of peaks. The differences can be due mainly to the geometry optimization process, which was not the same in both cases and could lead to differences in the electronic structure, hence the excited state properties. Nevertheless, in a more global view in Figure S8 (b), it can be seen that the general behaviour of the spectrum is reproduced and the absorption peak of the ligands around 6.5 eV is retrieved. These results motivate further analysis of the spectrum of $Au_{144}(SCH_2Ph)_{60}$ in the visible region in the future, which are beyond the scope of the present work. For all GNCs, computed spectra with a different type of ligands (hexyl or simplified -H terminations) show similar absorption profile in the visible region, only with a shift/intensity change of the bands (see Figure S9). In particular, replacing -H with the complete model of the ligands produces a systematic red-shift of 0.1-0.2 eV.

For a deeper analysis of the spectra presented, we show hole and electron densities corresponding to the lower excitation energy for $Au_{25}(SC_2H_4Ph)_{18}^-$, $Au_{38}(SC_2H_4Ph)_{24}$, Au_{102}(p-MBA)$_{44}$ and $Au_{144}(SCH_2Ph)_{60}$, in Figures 3 (e), (f), (g) and (h), respectively. These densities are obtained by tracking the population of each atomic orbital throughout the real-time dynamics, where a continuous laser perturbation is applied in tune with the excitation of interest (as explained in the computational methods). By doing so, we obtain an orbital-resolved picture of the electronic transitions, which allows us to better understand the nature of the excitations observed in the absorption spectra. The hole and electron densities for the lower excitation energy at 1.29 eV of $Au_{25}(SC_2H_4Ph)_{18}^-$ (Fig. 3 (e)) show a main localization in the Au_{13} core and sulphur atoms of the cluster with a negligible participation of the organic ligands. Furthermore, gold *sp* orbitals are the more relevant contributions to the hole and electron densities, which is in good agreement with previous TD-DFT calculations that propose this excitation as a major *sp* to *sp* intraband transition.[2] We also show that sulphur *p* orbitals has a significant contribution to the hole and electron densities. All these three observations are in good agreement with the calculations shown by Zhu, et al., and suggest that the lower energy excitation is a core gold transition.[2] Similarly, the hole and electron densities for the lower excitation energy of $Au_{38}(SC_2H_4Ph)_{24}$ are composed for gold atoms on the bi-icosahedral core with almost not participation of the ligands (see Fig. 3). Furthermore, gold *sp* orbitals and sulphur *p* orbitals are the more relevant contributions to the hole and electron densities, which is also in good agreement with the calculations by Pei, et al., that proposed this excitation as a major *sp* to *sp* intraband transition within the biicosahedral core. As can be expected taking into account the previous observations on the series, hole and electron densities at the lower energy transition for Au_{102}(p-MBA)$_{44}$ and $Au_{144}(SCH_2Ph)_{60}$ demonstrate that these peaks arise fundamentally from transitions between states that are mainly composed of *sp* orbitals from the gold core atoms and *p* from the sulphur atoms. Furthermore, for all the clusters, the contribution of *d* orbitals from gold atoms to the densities are the second main contribution after *sp* orbitals, as previously reported in previous DFT studies.[2,18]

The absorption signature of ligands can sometimes still be distinguished experimentally despite the wide absorption profile of large GNCs. As an example of such behavior, we detailed the UV-visible-nearIR spectrum of Au_{102}(p-MBA)$_{44}$ along with its hydrogen coated structure in Figure 4. The spectrum for Au_{102}(p-MBA)$_{44}$ in red shows a decay-like curve, which is almost identical to the $Au_{102}(SH)_{44}$ in black, except for a minor peak at 252 nm. This peak could be attributed to the aromatic carboxilated ligand, in agreement with previous experiments that have reported a peak at 269 nm for this system.[10,66] The hole and electron densities obtained after excitation at 252 nm are shown in Figure 4 (b). The percentages indicate a clear contribution of the organic ligands to the hole and electron densities (45.2% and 66%, respectively). These values are detailed per type of atomic orbital in Table S3. These results

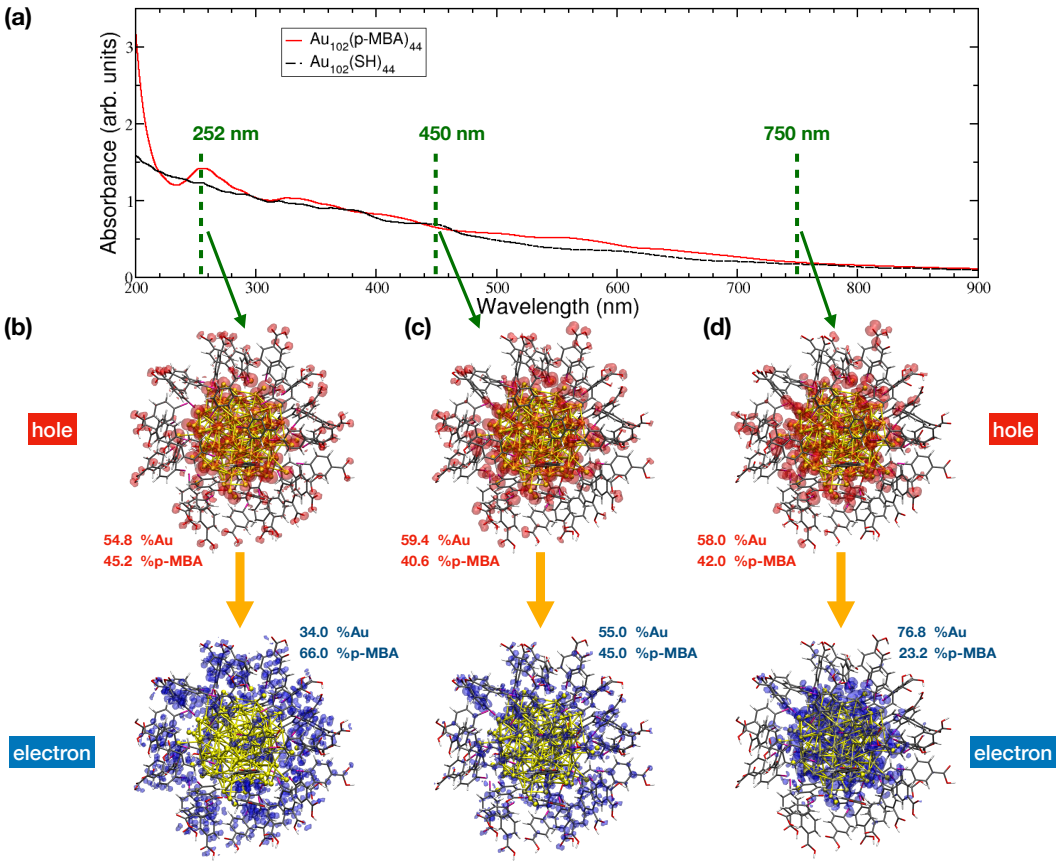

Figure 4: (a) Absorption spectra computed with RT-TD-DFTB in vacuum of $Au_{102}(SH)_{44}$ and Au_{102}(p-MBA)$_{44}$. (b, c, d) Hole/electron densities (isovalue $= 1.10^{-4}$) of selected absorption regions. The simulation of both absorption spectra were carried out up to 40000 steps using time step of 0.0048 fs and a field strength of 0.001 a.u. (equivalent to 1.33x10^7 W/cm^2). The laser dynamics at 252, 450 and 750 nm were carried out with an electron dymanics up to 20000 steps using the same time step and field strength as for the spectra. The hole/electron densities correspond to a snapshot at 90 fs of the electron dynamics.

confirm the previous experimental hypothesis that the small peak at 252 nm in the spectrum of Au_{102}(p-MBA)$_{44}$ is due to the presence of p-MBA molecules.[10,66] The cluster core also contributes significantly to the density, which is expected as this energy region involves many transitions involving the metallic part, as observed in the spectrum of $Au_{102}(SH)_{44}$ in Figure 4(a).

A further analysis of the excitations at lower energies (450 nm and 750 nm in Figures 4(c) and (d), respectively), shows that there is a low decay but there is still a significant contribution from the molecules to the hole densities (42.0% at 750 nm). In contrast, p-MBA contribution shows a more pronounced decrease in the case of the electron densities towards lower energies (23.2% at 750 nm). This asymmetric behaviour of the ligands contributions to the hole and electron densities at different wavelengths is due to the the presence of many states of the molecules in the valence band near the fermi level (see pDOS in Figure 2 (c)). Indeed, transitions involving occupied and non-occupied ligands states are only possible at high energies (short wavelengths). At lower energies (longer wavelengths), transitions are more likely to occur involving non-occupied states of the gold core Figure (2 (c)). These results suggest that the p-MBA molecules not only participate in the excitation at 252 nm but also far from the UV, *i.e.* in the visible and near-IR regions. The fact that the phenyl ring is directly linked to

the sulphur atom in the ligand may play a role in the coupling of the molecule states and the valence band edge since there is no insulating sp^3 carbon bridging them. Noteworthy, this analysis is based on the *auorg* parameterization of DFTB, relying on a GGA functional, and complementary works would be necessary to explore the potential improvements when working in a Long-range Corrected DFTB (LC-DFTB) framework, that is now only parameterized for organic atoms and is in principle better suited to treat charge-transfer excitations.[70] The wavelength dependence on the spatial charge separation under illumination opens the door for tuning the charge transfer (even catalytic) properties of this cluster by choosing the light source. Additionally, the effect may also depends on the ligand nature, so one may be able to chemically engineer the organic coat by, *e.g.*, changing or adding functional groups, to modify not only the optical absorption properties but also the space charge separation under photoexcitation. In principle, one could design a new "p-MBA ligand" that interact mostly with the conduction band giving rise to the opposite effect as the one described above. This principle could also be extended to the p-MBA coated versions of the other clusters of the series.

Conclusions

This work presents the first comprehensive evaluation of the DFTB and (LR/RT)TD-DFTB methods for describing the ground and excited states of gold nanoclusters (GNCs) fully coated with organic ligands, with sizes up to a thousand atoms. The GNCs studied were $Au_{25}(SR)_{18}^-$, $Au_{38}(SR)_{24}$, $Au_{102}(SR)_{44}$, and $Au_{144}(SR)_{60}$. We show that DFTB allows to reproduce the experimental observations and reference calculations. Specifically, the geometrical arrangement of the cluster along the series is correctly retrieved compared to crystallographic data. A low RMSD of the atoms positions is globally obtained, though the accuracy of the Au-Au bond lengths description clearly depends on the environment (core of the cluster or outer shell). The change in the electronic structure (decrease of the electronic gap) with the increase of the size of GNCs is retrieved along with a significant modification of the shape of the UV-Visible absorption spectra, from a well resolved molecular like bands for $Au_{25}(SR)_{18}^-$ and $Au_{38}(SR)_{24}$ to a semi-conductor like continuously increasing absorption for $Au_{102}(SR)_{44}$ and $Au_{144}(SR)_{60}$. The results obtained are in good agreement with previous experimental and theoretical studies. The nature of the low energy absorption band is tracked within the different GNCs, showing a similar character (mainly *sp* to *sp* of Au/S bands). In particular, RT-TD-DFTB calculations are able to accurately reproduce the position of the absorption band corresponding to the organic ligand shell when it is clearly visible experimentally, as demonstrated in the case of $Au_{102}(p\text{-}MBA)_{44}$. The results show that the ligands contribute significantly to the hole and electron densities, even at longer wavelengths. The wavelength dependence on the spatial charge separation under illumination suggests that one could tune the charge transfer properties of the cluster by choosing the energy source. The ability of the DFTB models to describe the structure and optical response of ligands protected GNCs constitutes an important step towards future computer-assisted design of GNC-based hybrid nanomaterial using a non expensive quantum chemistry method.

Nevertheless, from our results, further potential developments are identified to finely tune the *Auorg* DFTB parameterization. To better reproduce the heterogeneous Au-Au and Au-S bond distances, one possible strategy would be to have two sub-types of gold atoms (core and shell), with their respectively tuned parameters. Electronic parameters of the sulfur are to be corrected for a better description of the high energy unoccupied levels, if needed. Finally, the impact of the inclusion of Long-range corrections (LC-DFTB) in the treatment of the electronic excitations is to be unraveled and constitutes another promising way of improvement of the description of the photoinduced processes.

Supporting Information

Comparison of DFTB and DFT geometries, electronic gaps and density of states for the different GNCs, computed DFTB density of states for GNCs with various ligands, comparison of LR and RT TD-DFTB computed spectra for $Au_{25}(SC_2H_4Ph)_{18}^-$ and $Au_{38}(SC_2H_4Ph)_{24}$, comparison of the DFTB and experimental spectra for the different GNCs, computed DFTB spectra for the different GNCs with various ligands, detailled DFTB population analysis for selected excitations in Au_{102}(p-MBA)$_{44}$ spectrum.

Conflicts of interest

The authors declare no conflict of interest.

Acknowledgements

A. F is grateful for the support of the ANR FALCON project, grant ANR-20-CE09-0002-01 of the French *Agence Nationale de la Recherche*, and for the calculation resources support through the French GENCI agency at the CINES and IDRIS centers (grants: A0100800649 and AD010800649R1). C.R.L.-M. acknowledges the support from a DFG-RTG2247 grant (RTG-QM3 Program) for the postdoctoral fellowship and the high-computing resources of the BCCMS, University of Bremen.

References

(1) Du, Y.; Sheng, H.; Astruc, D.; Zhu, M. Atomically Precise Noble Metal Nanoclusters as Efficient Catalysts: A Bridge between Structure and Properties. *Chem. Rev.* **2020**, *120*, 526–622.

(2) Zhu, M.; Aikens, C. M.; Hollander, F. J.; Schatz, G. C.; Jin, R. Correlating the Crystal Structure of A Thiol-Protected Au25 Cluster and Optical Properties. *J. Am. Chem. Soc.* **2008**, *130*, 5883–5885.

(3) Matus, M. F.; Häkkinen, H. Understanding ligand-protected noble metal nanoclusters at work. *Nature Reviews Materials* **2023**, *8*, 372–389.

(4) Abbas, M. A.; Kamat, P. V.; Bang, J. H. Thiolated Gold Nanoclusters for Light Energy Conversion. *ACS Energy Letters* **2018**, *3*, 840–854.

(5) Abbas, M. A.; Jeon, M.; Bang, J. H. Understanding the Photoelectrochemical Behavior of Metal Nanoclusters: A Perspective. *The Journal of Physical Chemistry C* **2022**, *126*, 16928–16942.

(6) Du, X.; Jin, R. Atomically Precise Metal Nanoclusters for Catalysis. *ACS Nano* **2019**, *13*, 7383–7387.

(7) Naveen, M. H.; Khan, R.; Bang, J. H. Gold Nanoclusters as Electrocatalysts: Atomic Level Understanding from Fundamentals to Applications. *Chemistry of Materials* **2021**, *33*, 7595–7612.

(8) Cui, H.; Shao, Z.-S.; Song, Z.; Wang, Y.-B.; Wang, H.-S. Development of gold nanoclusters: from preparation to applications in the field of biomedicine. *J. Mater. Chem. C* **2020**, *8*, 14312–14333.

(9) Porret, E.; Le Guével, X.; Coll, J.-L. Gold nanoclusters for biomedical applications: toward in vivo studies. *J. Mater. Chem. B* **2020**, *8*, 2216–2232.

(10) Jin, R. Atomically precise metal nanoclusters: stable sizes and optical properties. *Nanoscale* **2015**, *7*, 1549–1565.

(11) Wu, Z.; Suhan, J.; Jin, R. One-pot synthesis of atomically monodisperse, thiol-functionalized Au_{25} nanoclusters. *J. Mater. Chem.* **2009**, *19*, 622–626.

(12) Heaven, M. W.; Dass, A.; White, P. S.; Holt, K. M.; Murray, R. W. Crystal Structure of the Gold Nanoparticle $[N(C_8H_{17})_4][Au_{25}(SCH_2CH_2Ph)_{18}]$. *Journal of the American Chemical Society* **2008**, *130*, 3754–3755.

(13) Qian, H.; Zhu, M.; Wu, Z.; Jin, R. Quantum Sized Gold Nanoclusters with Atomic Precision. *Accounts of Chemical Research* **2012**, *45*, 1470–1479.

(14) Zhu, M.; Eckenhoff, W. T.; Pintauer, T.; Jin, R. Conversion of Anionic $[Au_{25}(SCH_2CH_2Ph)_{18}]$ Cluster to Charge Neutral Cluster via Air Oxidation. *The Journal of Physical Chemistry C* **2008**, *112*, 14221–14224.

(15) Venzo, A.; Antonello, S.; Gascón, J. A.; Guryanov, I.; Leapman, R. D.; Perera, N. V.; Sousa, A.; Zamuner, M.; Zanella, A.; Maran, F. Effect of the Charge State (z = 1, 0, +1) on the Nuclear Magnetic Resonance of Monodisperse Au_{25}[S(CH2)2Ph]$_{18}$z Clusters. *Analytical Chemistry* **2011**, *83*, 6355–6362.

(16) Liu, Z.; Zhu, M.; Meng, X.; Xu, G.; Jin, R. Electron Transfer between $[Au_{25}(SC_2H_4Ph)_{18}]$TOA+ and Oxoammonium Cations. *The Journal of Physical Chemistry Letters* **2011**, *2*, 2104–2109.

(17) Jiang, D.-e.; Tiago, M. L.; Luo, W.; Dai, S. The "Staple" Motif: A Key to Stability of Thiolate-Protected Gold Nanoclusters. *Journal of the American Chemical Society* **2008**, *130*, 2777–2779.

(18) Pei, Y.; Gao, Y.; Zeng, X. C. Structural Prediction of Thiolate-Protected Au_{38}: A Face-Fused Bi-icosahedral Au Core. *Journal of the American Chemical Society* **2008**, *130*, 7830–7832.

(19) Qian, H.; Eckenhoff, W. T.; Zhu, Y.; Pintauer, T.; Jin, R. Total Structure Determination of Thiolate-Protected Au38 Nanoparticles. *J. Am. Chem. Soc.* **2010**, *132*, 8280–8281.

(20) Jung, J.; Kang, S.; Han, Y.-K. Ligand effects on the stability of thiol-stabilized gold nanoclusters: $Au_{25}(SR)_{18}$, $Au_{38}(SR)_{24}$, and $Au_{102}(SR)_{44}$. *Nanoscale* **2012**, *4*, 4206–4210.

(21) Guo, R.; Murray, R. W. Substituent Effects on Redox Potentials and Optical Gap Energies of Molecule-like Au38(SPhX)24 Nanoparticles. *Journal of the American Chemical Society* **2005**, *127*, 12140–12143.

(22) Lee, D.; Donkers, R. L.; Wang, G.; Harper, A. S.; Murray, R. W. Electrochemistry and Optical Absorbance and Luminescence of Molecule-like Au_{38} Nanoparticles. *Journal of the American Chemical Society* **2004**, *126*, 6193–6199.

(23) Jadzinsky, P. D.; Calero, G.; Ackerson, C. J.; Bushnell, D. A.; Kornberg, R. D. Structure of a Thiol Monolayer-Protected Gold Nanoparticle at 1.1 Å Resolution. *Science* **2007**, *318*, 430–433.

(24) Gao, Y.; Shao, N.; Zeng, X. C. Ab Initio Study of Thiolate-Protected Au_{102} Nanocluster. *ACS Nano* **2008**, *2*, 1497–1503.

(25) Lopez-Acevedo, O.; Akola, J.; Whetten, R. L.; Grönbeck, H.; Häkkinen, H. Structure and Bonding in the Ubiquitous Icosahedral Metallic Gold Cluster $Au_{144}(SR)_{60}$. *The Journal of Physical Chemistry C* **2009**, *113*, 5035–5038.

(26) Yan, N.; Xia, N.; Liao, L.; Zhu, M.; Jin, F.; Jin, R.; Wu, Z. Unraveling the long-pursued Au_{144} structure by x-ray crystallography. *Science Advances* **2018**, *4*, eaat7259.

(27) Aikens, C. M. Effects of Core Distances, Solvent, Ligand, and Level of Theory on the TDDFT Optical Absorption Spectrum of the Thiolate-Protected Au_{25} Nanoparticle. *The Journal of Physical Chemistry A* **2009**, *113*, 10811–10817.

(28) Day, P. N.; Nguyen, K. A.; Pachter, R. Calculation of one-and two-photon absorption spectra of thiolated gold nanoclusters using time-dependent density functional theory. *Journal of Chemical Theory and Computation* **2010**, *6*, 2809–2821.

(29) Sinha-Roy, R.; López-Lozano, X.; Whetten, R. L.; Weissker, H.-C. Crucial Role of Conjugation in Monolayer-Protected Metal Clusters with Aromatic Ligands: Insights from the Archetypal Au144L60 Cluster Compounds. *The Journal of Physical Chemistry Letters* **2021**, *12*, 9262–9268, PMID: 34533967.

(30) Elstner, M.; Porezag, D.; Jungnickel, G.; Elsner, J.; Haugk, M.; Frauenheim, T.; Suhai, S.; Seifert, G. Self-consistent-charge density-functional tight-binding method for simulations of complex materials properties. *Phys. Rev. B* **1998**, *58*, 7260–7268.

(31) Gaus, M.; Cui, Q.; Elstner, M. DFTB3: Extension of the Self-Consistent-Charge Density-Functional Tight-Binding Method (SCC-DFTB). *J. Chem. Theory Comput.* **2011**, *7*, 931–948.

(32) Fihey, A.; Hettich, C.; Touzeau, J.; Maurel, F.; Perrier, A.; Köhler, C.; Aradi, B.; Frauenheim, T. SCC-DFTB parameters for simulating hybrid gold-thiolates compounds. *J. Comput. Chem.* **2015**, *36*, 2075–2087.

(33) Oliveira, L. F. L.; Tarrat, N.; Cuny, J.; Morillo, J.; Lemoine, D.; Spiegelman, F.; Rapacioli, M. Benchmarking Density Functional Based Tight-Binding for Silver and Gold Materials: From Small Clusters to Bulk. *J. Phys. Chem. A* **2016**, *120*, 8469–8483.

(34) Douglas-Gallardo, O. A.; Berdakin, M.; Frauenheim, T.; Sánchez, C. G. Plasmon-induced hot-carrier generation differences in gold and silver nanoclusters. *Nanoscale* **2019**, *11*, 8604–8615.

(35) Domínguez-Castro, A.; Lien-Medrano, C. R.; Maghrebi, K.; Messaoudi, S.; Frauenheim, T.; Fihey, A. Photoinduced charge-transfer in chromophore-labeled gold nanoclusters: quantum evidence of the critical role of ligands and vibronic couplings. *Nanoscale* **2021**, *13*, 6786–6797.

(36) Vuong, V. Q.; Madridejos, J. M. L.; Aradi, B.; Sumpter, B. G.; Metha, G. F.; Irle, S. Density-functional tight-binding for phosphine-stabilized nanoscale gold clusters. *Chem. Sci.* **2020**, *11*, 13113–13128.

(37) Niehaus, T. A.; Suhai, S.; Della Sala, F.; Lugli, P.; Elstner, M.; Seifert, G.; Frauenheim, T. Tight-binding approach to time-dependent density-functional response theory. *Physical Review B* **2001**, *63*, 085108.

(38) Bonafé, F. P.; Aradi, B.; Hourahine, B.; Medrano, C. R.; Hernández, F. J.; Frauenheim, T.; Sánchez, C. G. A Real-Time Time-Dependent Density Functional Tight-Binding Implementation for Semiclassical Excited State Electron–Nuclear Dynamics and Pump–Probe Spectroscopy Simulations. *Journal of Chemical Theory and Computation* **2020**, *16*, 4454–4469.

(39) Elstner, M.; Seifert, G. Density functional tight binding. *Philosophical Transactions of the Royal Society A: Mathematical, Physical and Engineering Sciences* **2014**, *372*, 20120483.

(40) Christensen, A. S.; Kubař, T.; Cui, Q.; Elstner, M. Semiempirical Quantum Mechanical Methods for Noncovalent Interactions for Chemical and Biochemical Applications. *Chemical Reviews* **2016**, *116*, 5301–5337.

(41) Hourahine, B. et al. DFTB+, a software package for efficient approximate density functional theory based atomistic simulations. *The Journal of Chemical Physics* **2020**, *152*, 124101.

(42) Casida, M. E. *Recent Advances in Density Functional Methods*; 1995; Chapter Time-Dependent Density Functional Response Theory for Molecules, pp 155–192.

(43) Yabana, K.; Bertsch, G. Time-dependent local-density approximation in real time. *Phys. Rev. B* **1996**, *54*, 4484–4487.

(44) Castro, A.; Appel, H.; Oliveira, M.; Rozzi, C. A.; Andrade, X.; Lorenzen, F.; Marques, M. A. L.; Gross, E. K. U.; Rubio, A. Octopus: a Tool for the Application of Time-Dependent Density Functional Theory. *Phys. Status Solidi* **2006**, *243*, 2465–2488.

(45) Onida, G.; Reining, L.; Rubio, A. Electronic excitations: density-functional versus many-body Green's-function approaches. *Rev. Mod. Phys.* **2002**, *74*, 601–659.

(46) Frisch, M. J. et al. Gaussian 16 Revision C.01. 2016; Gaussian Inc. Wallingford CT.

(47) Heinecke, C. L.; Ni, T. W.; Malola, S.; Mäkinen, V.; Wong, O. A.; Häkkinen, H.; Ackerson, C. J. Structural and Theoretical Basis for Ligand Exchange on Thiolate Monolayer Protected Gold Nanoclusters. *J. Am. Chem. Soc.* **2012**, *134*, 13316–13322.

(48) Walter, M.; Akola, J.; Lopez-Acevedo, O.; Jadzinsky, P. D.; Calero, G.; Ackerson, C. J.; Whetten, R. L.; Grönbeck, H.; Häkkinen, H. A unified view of ligand-protected gold clusters as superatom complexes. *Proceedings of the National Academy of Sciences* **2008**, *105*, 9157–9162.

(49) Qian, H.; Jin, R. Controlling Nanoparticles with Atomic Precision: The Case of Au144(SCH2CH2Ph)60. *Nano Lett.* **2009**, *9*, 4083–4087.

(50) Ackerson, C. J.; Jadzinsky, P. D.; Sexton, J. Z.; Bushnell, D. A.; Kornberg, R. D. Synthesis and bioconjugation of 2 and 3 nm-diameter gold nanoparticles. *Bioconjugate Chemistry* **2010**, *21*, 214–218.

(51) Malola, S.; Nieminen, P.; Pihlajamäki, A.; Hämäläinen, J.; Kärkkäinen, T.; Häkkinen, H. A method for structure prediction of metal-ligand interfaces of hybrid nanoparticles. *Nature Communications* **2019**, *10*, 3973.

(52) Li, Y.; Galli, G.; Gygi, F. Electronic Structure of Thiolate-Covered Gold Nanoparticles: Au102(MBA)44. *ACS Nano* **2008**, *2*, 1896–1902.

(53) Weissker, H. C.; Escobar, H. B.; Thanthirige, V. D.; Kwak, K.; Lee, D.; Ramakrishna, G.; Whetten, R. L.; López-Lozano, X. Information on quantum states pervades the visible spectrum of the ubiquitous $Au_{144}(SR)_{60}$ gold nanocluster. *Nature Communications* **2014**, *5*, 1–8.

(54) Qian, H.; Jin, R. Ambient Synthesis of $Au_{144}(SR)_{60}$ Nanoclusters in Methanol. *Chemistry of Materials* **2011**, *23*, 2209–2217.

(55) Lopez-Acevedo, O.; Tsunoyama, H.; Tsukuda, T.; Häkkinen, H.; Aikens, C. M. Chirality and Electronic Structure of the Thiolate-Protected Au_{38} Nanocluster. *Journal of the American Chemical Society* **2010**, *132*, 8210–8218.

(56) Akola, J.; Walter, M.; Whetten, R. L.; Häkkinen, H.; Grönbeck, H. On the Structure of Thiolate-Protected Au_{25}. *Journal of the American Chemical Society* **2008**, *130*, 3756–3757.

(57) Jin, R. Quantum sized, thiolate-protected gold nanoclusters. *Nanoscale* **2010**, *2*, 343–362.

(58) Qian, H.; Zhu, Y.; Jin, R. Size-Focusing Synthesis, Optical and Electrochemical Properties of Monodisperse $Au_{38}(SC_2H_4Ph)_{24}$ Nanoclusters. *ACS Nano* **2009**, *3*, 3795–3803.

(59) Chen, Y.; Wang, J.; Liu, C.; Li, Z.; Li, G. Kinetically controlled synthesis of $Au_{102}(SPh)_{44}$ nanoclusters and catalytic

application. *Nanoscale* **2016**, *8*, 10059–10065.

(60) Koivisto, J.; Salorinne, K.; Mustalahti, S.; Lahtinen, T.; Malola, S.; Häkkinen, H.; Pettersson, M. Vibrational Perturbations and Ligand–Layer Coupling in a Single Crystal of $Au_{144}(SC_2H_4Ph)_{60}$ Nanocluster. *The Journal of Physical Chemistry Letters* **2014**, *5*, 387–392.

(61) Hicks, J. F.; Miles, D. T.; Murray, R. W. Quantized Double-Layer Charging of Highly Monodisperse Metal Nanoparticles. *Journal of the American Chemical Society* **2002**, *124*, 13322–13328.

(62) Quinn, B. M.; Liljeroth, P.; Ruiz, V.; Laaksonen, T.; Kontturi, K. Electrochemical Resolution of 15 Oxidation States for Monolayer Protected Gold Nanoparticles. *Journal of the American Chemical Society* **2003**, *125*, 6644–6645.

(63) Koivisto, J.; Malola, S.; Kumara, C.; Dass, A.; Häkkinen, H.; Pettersson, M. Experimental and Theoretical Determination of the Optical Gap of the $Au_{144}(SC_2H_4Ph)_{60}$ Cluster and the $(Au/Ag)_{144}(SC_2H_4Ph)_{60}$ Nanoalloys. *The Journal of Physical Chemistry Letters* **2012**, *3*, 3076–3080.

(64) Niehaus, T. A. Approximate time-dependent density functional theory. *Journal of Molecular Structure: THEOCHEM* **2009**, *914*, 38–49.

(65) Tsunoyama, H.; Nickut, P.; Negishi, Y.; Al-Shamery, K.; Matsumoto, Y.; Tsukuda, T. Formation of Alkanethiolate-Protected Gold Clusters with Unprecedented Core Sizes in the Thiolation of Polymer-Stabilized Gold Clusters. *The Journal of Physical Chemistry C* **2007**, *111*, 4153–4158.

(66) Levi-Kalisman, Y.; Jadzinsky, P. D.; Kalisman, N.; Tsunoyama, H.; Tsukuda, T.; Bushnell, D. A.; Kornberg, R. D. Synthesis and Characterization of Au_{102}(p-MBA)$_{44}$ Nanoparticles. *Journal of the American Chemical Society* **2011**, *133*, 2976–2982.

(67) Hulkko, E.; Lopez-Acevedo, O.; Koivisto, J.; Levi-Kalisman, Y.; Kornberg, R. D.; Pettersson, M.; Häkkinen, H. Electronic and Vibrational Signatures of the Au_{102}(p-MBA)$_{44}$ Cluster. *Journal of the American Chemical Society* **2011**, *133*, 3752–3755.

(68) Chaki, N. K.; Negishi, Y.; Tsunoyama, H.; Shichibu, Y.; Tsukuda, T. Ubiquitous 8 and 29 kDa gold:alkanethiolate cluster compounds: Mass-spectrometric determination of molecular formulas and structural implications. *Journal of the American Chemical Society* **2008**, *130*, 8608–8610.

(69) Qian, H.; Jin, R. Controlling nanoparticles with atomic precision: The case of $Au_{144}(SCH_2CH_2Ph)_{60}$. *Nano Letters* **2009**, *9*, 4083–4087.

(70) Vuong, V. Q.; Akkarapattiakal Kuriappan, J.; Kubillus, M.; Kranz, J. J.; Mast, T.; Niehaus, T. A.; Irle, S.; Elstner, M. Parametrization and Benchmark of Long-Range Corrected DFTB2 for Organic Molecules. *J. Chem. Theory Comput.* **2018**, *14*, 115–125.